Wesleyan University
WesScholar

Division III Faculty Publications | Natural Sciences and Mathematics

January 2011

Stability of DNA-linked nanoparticle crystals I: Effect of linker sequence and length

Francis W. Starr
Wesleyan University, fstarr@wesleyan.edu

Fernando Vargas Lara

Follow this and additional works at: http://wesscholar.wesleyan.edu/div3facpubs

Part of the Physics Commons

Recommended Citation
Starr, Francis W. and Vargas Lara, Fernando, "Stability of DNA-linked nanoparticle crystals I: Effect of linker sequence and length" (2011). *Division III Faculty Publications.* Paper 299.
http://wesscholar.wesleyan.edu/div3facpubs/299

This Article is brought to you for free and open access by the Natural Sciences and Mathematics at WesScholar. It has been accepted for inclusion in Division III Faculty Publications by an authorized administrator of WesScholar. For more information, please contact dschnaidt@wesleyan.edu, ljohnson@wesleyan.edu.

Soft Matter

Dynamic Article Links

Cite this: DOI: 10.1039/c0sm00989j

www.softmatter.org

PAPER

Stability of DNA-linked nanoparticle crystals I: Effect of linker sequence and length

Fernando Vargas Lara and Francis W. Starr*

Received 14th September 2010, Accepted 15th December 2010
DOI: 10.1039/c0sm00989j

The creation of three-dimensional, crystalline-ordered nanoparticle (NP) structures linked by DNA has proved experimentally challenging. Here we aim to systematically study parameters that influence the relative thermodynamic and kinetic stability of such crystals. To avoid experimental bottlenecks and directly control molecular-scale parameters, we carry out molecular dynamics simulations of a coarse-grained model in which short DNA strands (6 to 12 bp) are tethered to a NP core. We examine the influence of the number of bases per strand L, number of linking bases ℓ and the number of spacer bases s on the stability of crystal states. We also consider the effect of using a single linking NP type *versus* a binary linking system. We explicitly compute the free energy, entropy, and melting point T_M for BCC and FCC lattices. We show that binary systems are preferable for generating BCC lattices, while a single NP type generates the most stable FCC crystals. We propose a simple model for short DNA strands that can account for T_M of all our data. The model also indicates that the heat of fusion between crystal and amorphous phases grows linearly with ℓ, providing a route to maximize the relative crystal stability.

1 Introduction

The development of DNA as a building block for the production of nanomaterials has gained increasing attention due to the particular properties of DNA, such as sequence-specific binding, cooperativity of double-helix hybridization, the reversibility of bonding, and the tunability of interaction strength (by varying the relative number of A–T and C–G pairs).[1–3] Moreover, double helices of DNA are relatively rigid over length scales approaching 100 nm, so that double-stranded DNA (dsDNA) may act as "beams" connecting a larger scale networked structure. Such complex DNA-linked networks require the effectively 1D stands to be linked by junctions. One popular approach to create junctions is to attach a number of single strands of DNA (ssDNA) to a core particle.[4–6] By appropriate choice of base sequences, the functionalized NP can self-assemble by the formation of dsDNA links. This approach has been experimentally studied for both colloidal[7–15] and NP[6,16–28] core units, and in most cases it has been found that the particles form disordered aggregates.

For many applications, long-ranged crystal order, as opposed to amorphous order, is preferable, since such materials are expected to have unique electronic and optical properties which potentially can be used in the production of lasers, microscopes, and energy storage materials, among others.[29] However, the self-assembly of these DNA-linked NP into 3D macroscale ordered structures is a challenging task. Some recent experiments have succeeded to generate 3D crystalline DNA-functionalized NP.[25–28] In these experiments, gold NP were functionalized with strands of DNA that have a non-binding "spacer" near to the NP, and a "linking" region at the end of the strand that can hybridize with strands from other NP. These experiments found either body-centered cubic (BCC) or face-centered cubic (FCC) crystals, depending on the base sequence, length, and rigidity of the strands. Even with the success of these experiments, it is important to develop an improved understanding of how these parameters affect the formation of crystal states and their relative stability. Since there are a large number of parameters to vary, it is important to be able to address each one in an independent way. However, direct experimental testing of all parameters is particularly challenging. Alternatively, if we have an appropriate model, it is straightforward to vary these parameters individually.

Accordingly, we present simulation results from a coarse-grained molecular model in which we can explicitly evaluate the crystal stability and how it varies with possible design choices. Specifically, we test how the relative number of bases of the spacer and linking regions, and the DNA sequence affects both the thermodynamic and kinetic stability of crystal states (for strands smaller or on the order of the ssDNA persistence length).

We find that for NP functionalized with short DNA strands (6 to 12 bp), the stability increases with increasing length of the linking region, a result of the cooperative nature of DNA zipping. Our thermodynamic analysis shows that effects of

Department of Physics, Wesleyan University, Middletown, Connecticut, 06459, USA. E-mail: fstarr@wesleyan.edu

metastability are minimal; that is, super-heating of crystal states does not readily occur. This is understood from the fact the hybridization of DNA that binds the NP typically has no hysteresis. The stability of the crystal states decreases with increasing the length of the spacer region, which can be understood from a simple model for the NP links. We combine these results to offer a simple model that can explain the variation of T_M on all parameters for the case of short strands.

The paper is organized as follows: in section 2, the coarse-grained model and the cases that we study are explained in detail; section 3 presents the thermodynamic integration method with the variations that we use to compute the thermodynamic parameters; in sections 4 and 5, we present how the system type and the number of spacers and linkers affect the crystal stability. We conclude briefly in section 6.

2 Model and simulation methods

Explicit atomistic models for DNA-functionalized NP, where thousands of DNA bases are involved, represent a major computational challenge. These atom-based models require a very large number of force sites, so that even a recent state-of-the-art calculation is limited to just one DNA-functionalized NP with four ssDNA, where each ssDNA is composed of ten bases.[30] In order to overcome these limitations, we use a simple coarse-grained generalization of a model originally developed for tetrahedrally functionalized NP.[31] Previously, it has been shown that the model captures many of the salient features of DNA-driven assembly.[32–36]

In this model, each nucleotide is represented by two force sites, one for the phosphate-sugar backbone (monomer site) and one for the nitrogenous base (sticky site). The backbone provides connectivity; the sticky site carries the information to make bridges between complementary bases (A–T and C–G) of different strands. For the steric repulsion of the DNA strand backbone, we use a Weeks-Chandler-Andersen potential (WCA), which is related to a force-shifted Lennard Jones potential (LJ),

$$U(r) = U_{LJ}(r) - U_{LJ}(r_c) - (r - r_c)\frac{dU_{LJ}}{dr}\Big|_{r=r_c}, \quad (1)$$

where r_c is a cutoff distance for the potential. The LJ potential has a characteristic energy ε, and particle core size σ. For the WCA potential, eqn (1) is truncated at the minimum of the LJ potential ($r_c = 2^{\frac{1}{6}}\sigma$), so that interactions are purely repulsive. Additionally, each force site has mass m. For the remaining discussion, we use reduced units where length is given in units of σ and energy in units of ε; temperature is expressed in units of ε/k_B (k_B is the Boltzmann constant), entropy in units of k_B and time in units of $\sigma\sqrt{m/\varepsilon}$.

The connectivity of the backbone monomers is provided by the finitely extensible, nonlinear-elastic (FENE) anharmonic spring potential,

$$U_{\mathrm{FENE}}(r) = -\frac{kR_0^2}{2}\ln\left[1 - \left(\frac{r}{R_0}\right)^2\right], \quad (2)$$

where the bond strength $k = 30\varepsilon/\sigma^2$ and the maximum bond extension $R_0 = 1.5\sigma$. In addition, a three-body bending potential

$$U_{\mathrm{lin}}(r) = k_{\mathrm{lin}}(1 + \cos\theta), \quad (3)$$

where θ is the angle defined by three consecutive monomers and k_{lin} is the bending constant, provides the chain the characteristic rigidity of the DNA strands. To fix the value of k_{lin}, we wish to approximately match the experimentally known persistence length of ssDNA. Specifically, we compute the orientational correlation function of the backbone monomers from the scalar product of two unitary vectors $\langle \vec{u_i}.\vec{u_j} \rangle$ where $\vec{u_i}$ is defined by the bond connectivity between backbone monomers i and $i + 1$. The orientational correlation function shows an exponential decay

$$\left\langle \vec{u_i}.\vec{u_j} \right\rangle = \exp\left(-\frac{|s_i - s_j|}{l_p}\right) \quad (4)$$

from which we obtain the persistence length l_p.[37] Fig. 1 shows the effect k_{lin} on l_p for a single strand. We select $k_{\mathrm{lin}} = 3$ and also check $k_{\mathrm{lin}} = 1$ for several cases to test the impact of increased flexibility.

The attractive bases are represented by a small sticky site carrying the identity A, C, G or T. Each sticky site is connected to a monomer of the backbone chain using the same FENE potential (eqn (2)) linking the backbone monomers. We use the WCA potential between the sticky sites and the backbone, with $\sigma_s = 0.35\sigma$; in combination with the FENE potential, this choice holds the sticky site close to the backbone, which will be important to prevent multiple bonding of bases. Non-complementary sticky sites also interact *via* the WCA potential with $r_c = 2^{\frac{1}{6}}\sigma_s$ to avoid any attraction. Finally, complementary bases (*i.e.* A–T or C–G pairs) interact using the force-shifted LJ potential with $\sigma_s = 0.35\sigma$, truncated at $r_c = 2.5\sigma_s$ to include attraction. In this model, the bonding strength for A–T and C–G pairs is the same. The range of attraction is short enough that when a complementary pair is within the interaction range, the steric repulsion of the backbone to which the sticky site is attached will not allow for a third base to come close enough to interact, thereby preserving the one-to-one binding of DNA bases. At this level of complexity, the DNA model captures the zipper-like transition of DNA, but does not reproduce the

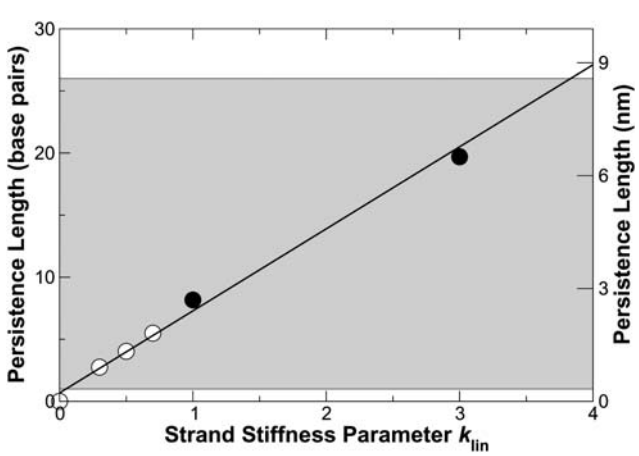

Fig. 1 The persistence length l_p for a single strand of the DNA model as a function of the chain-stiffening parameter k_{lin}. The gray region represents the range of experimentally measured l_p.[38–40] We choose $k_{\mathrm{lin}} = 3$ for most calculations, and check $k_{\mathrm{lin}} = 1$ for a few systems to test the impact of increased flexibility. $k_{\mathrm{lin}} = 1$ and $k_{\mathrm{lin}} = 3$ are shown with filled symbols.

This journal is © The Royal Society of Chemistry 2011

ART ■ C0SM00989J

helicity of DNA. More complex coarse-grained models are able to reproduce more detailed DNA structure,[41–43] but spontaneous hybridization of these models on simulation time scales remains a challenge.

We model each nanoparticle as a collection of 13 force sites bonded together using the FENE potential to form an icosahedral geometry. There is one force site at each of the 12 vertices of the icosahedron, and one at the center to maintain stability of the NP. Non-bonded interactions between core force sites, or with force sites of the DNA chains, are given by the WCA potential with $\sigma = 1.0$.

To create functionalized complexes, we tether one end of an ssDNA to each vertex, as illustrated in Fig. 2(a). Bonds between the NP core and the strand are also given by the FENE potential (eqn (2)). To maintain the orientation of the arms relative to the core, we use the three-body bending potential of eqn (3). Specifically, for each strand attachment, we use the three-body bending potential amongst the attaching backbone site of the chain, the NP vertex to which it attaches, and the NP central core force site. This results in chains which are roughly normal to the NP surface, consistent with the fully atomistic simulations of Schatz and co-workers[30] for ssDNA tethered to a gold NP.

We consider strands with L number of bases. The bases nearest the NP make up a non-binding "spacer" region of length s bases, and the outer bases of the chains have a specific "linking" sequence of length ℓ bases, that provides the possible connection between two NP (Fig. 2(a)). Obviously, $L = s + \ell$, and we consider values $s = 2$ or 4 and $\ell = 4$, 6, or 8, so that L varies from 6 to 12. The sequences have been chosen to try to maximize the energy difference between the fully linked strands and other possible partially bonded states, thereby decreasing the likelihood of partial bonding. Additionally, since our model does not distinguish the energy of A–T and C–G bonds, we select sequences where the binding-energy per base expected experimentally[44] differs by less than 5%, regardless of ℓ (Table 1). This allows us to readily compare systems with different ℓ.

We study two different types of possible NP functionalization. The first case we examine is when each NP is functionalized by identical strands with linker regions that are self-complementary in reverse order. As a result, strands attached to the same NP will not readily bind, but strands from different NP can link to build large aggregates. We refer to this as the NP1–NP1 linking case (Fig. 2(b) upper panel). The second case we consider is a binary system where two NP types have a linking sequence that will not bind to strands within the same NP, and are non-complementary to other NP of the same type. Thus NP of the same type cannot form aggregates. The sequences of different NP types are complementary, so that aggregates with a "checkboard" pattern, such as in a BCC crystal, are favored (Fig. 2(b) lower panel). We refer to this as the NP1–NP2 linking case.

Table 1 Linker sequences used in: (a) the NP1–NP1, and (b) the NP1–NP2 systems. We select sequences where the experimentally expected bonding energy per base differs by less than 5%, regardless of ℓ. We calculate the bonding energy per base based on the data from ref. 44

a) NP1–NP1	
number of linkers (ℓ)	NP1 Sequence
4	*GATC*
6	*GGTACC*
8	*GGTATACC*

b) NP1–NP2	
number of linkers (ℓ)	NP1 Sequence/NP2 Sequence
4	*TCTC/AGAG*
6	*TCTTCC/AGAAGG*
8	*TTTCAGGG/AAAGTCCC*

We study the model using molecular dynamics simulations in the temperature range $0.09 \leq T \leq 0.160$ at densities compatible with either an FCC or BCC lattice (Fig. 3). We use periodic boundary conditions. To control temperature, we use the Nose-Hoover method,[45] where T is defined from the mean kinetic energy. We integrate the equations of motion using a two level, three-cycle velocity Verlet version of the rRESPA multiple time-step algorithm,[46] with the forces separated into rapidly varying bonded forces and more slowly varying non-bonded forces. The time step for the bonded forces is 0.002.

The spontaneous formation of crystal states can be extremely slow in the simulations, and in many cases, spontaneous crystallization is not accessible in our simulation window.

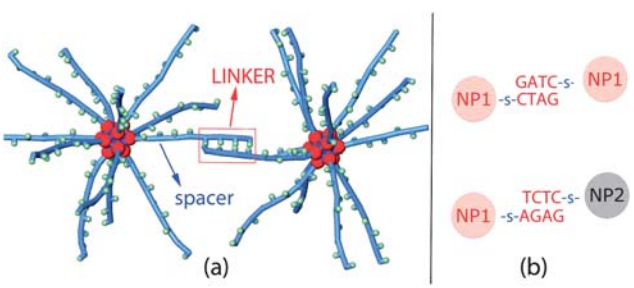

Fig. 2 (a) Snapshot of two icosahedral NP functionalized by 12 ssDNA. The cylinders represent the bonds of the backbone of a ssDNA and the small spheres are a coarse-grained representation of the nitrogen bases. The backbone monomers are not shown for purpose of clarity. At low T, two NP with complementary linker regions will be bound by spontaneously zipping of the strands. (b) Example of possible sequences for the NP1–NP1 system in the upper panel, and the NP1–NP2 system in the lower panel. Here the s represents the spacer region.

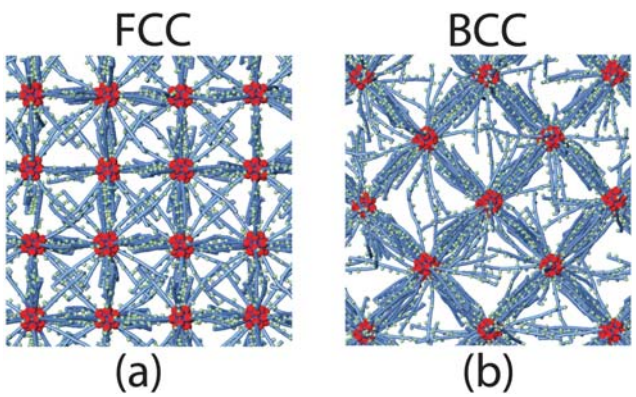

Fig. 3 Example of DNA functionalized nanoparticle lattices with: (a) FCC symmetry, NP1–NP1 interaction. Here, each ssDNA strand with $L = 6$ and $\ell = 4$; (b) BCC symmetry, NP1–NP2 interaction. Each ssDNA strand has $L = 8$ and $\ell = 6$.

ART ■ C0SM00989J

Fortunately, we can prepare an initial crystal state by constraining the location of the centers of the NP to the desired crystal locations. The lattice spacing is determined by the DNA binding length. We determine this length in preliminary simulations from the first neighbor NP separation, given by the pair correlation function $g(r)$ for an NP dimer. By equilibrating this constrained system at low T, dsDNA links between different NP will spontaneously form. The resulting crystal will be kinetically stable at sufficiently low T, but it may not be a thermodynamically stable state. We examine the stability by thermal studies after removing the constraint on the NP centers.

Since it is computationally costly to study the model for very large systems, we would like to use a minimal size that still provides a good estimate of the thermodynamic limit. Accordingly, we checked for finite size effects on the total energy and free energy for crystal systems by examining an increasing number of unit cells of NP with either BCC (up to 64 unit cells, or 128 functionalized NP) or FCC symmetry (up to 27 unit cells, or 108 functionalized NP). Our tests indicated no change in the free energy per NP for system sizes ≥8 unit cells of either BCC or FCC symmetry. Accordingly, we present results for systems with 8 unit cells.

3 Free energy calculation

We calculate the free energy using the thermodynamic integration method.[45] In this method, the free energy is calculated by parametrically coupling the potential energy of the system to the potential energy of a reference system for which the free energy can be directly, analytically evaluated.

Typically, the potentials are linearly coupled by a parameter λ, so that

$$U(\lambda) = (1 - \lambda)U_{\mathrm{DNA}} + \lambda U_{\mathrm{ref}}. \tag{5}$$

However, this linear coupling leads to unforeseen *numerical* problems when using the FENE bond potential. If the distance between two bonded particles exceeds the spacing R_0, the argument of the logarithm is negative, and the value of the potential becomes a non-real number. In principle, this should not occur, since the bonding force diverges approaching R_0. However, as λ approaches 1, the system is controlled almost entirely by the reference potential, and it becomes numerically possible for particles sharing a bond to exceed the preferred bond distance, unless an impractically-small time step is used. Practically speaking, using the potential described by eqn (5), it is difficult to achieve meaningful results for $\lambda \gtrsim 0.8$. To resolve this issue, we alter the coupling potential to make the bond potential more influential as $\lambda \to 1$. Specifically, we use

$$U(\lambda) = (1 - 0.1\lambda - 0.9\lambda^8)U_{\mathrm{DNA}} + (0.1\lambda + 0.9\lambda^8)U_{\mathrm{ref}}. \tag{6}$$

Following the standard procedure of thermodynamic integration, it is known that

$$\left(\frac{\partial F(\lambda)}{\partial \lambda}\right)_{N,V,T} = \left\langle \frac{\partial U(\lambda)}{\partial \lambda} \right\rangle_{\lambda}, \tag{7}$$

where F is the Helmholtz Free Energy. Integrating this result with respect to λ, and using eqn (6) we have

$$F_{\mathrm{DNA}} = F_{\mathrm{ref}} - \int_0^1 (7.2\lambda^7 + 0.1)\langle U_{\mathrm{ref}} - U_{\mathrm{DNA}}\rangle d\lambda. \tag{8}$$

The harmonic potential is the most commonly used reference potential for this type of calculation. However, since we use periodic boundary conditions, we can potentially have problems since the harmonic potential has no periodicity. To solve this issue, we could track and correct for the boundary crossings. Instead, we use a potential that shares the system periodicity,[47] namely

$$U_{\mathrm{ref}}(r) = -U_0 \sum_{i=1}^{3} \cos\left(\frac{2\pi}{V^{\frac{1}{3}}} r_i\right), \tag{9}$$

where U_0 is the amplitude of the potential, V is the volume of the container and r_i is the coordinate of particle i. For an N particle system interacting through U_{ref}, evaluation of the partition function shows that

$$F_{\mathrm{ref}} = \frac{3N}{\beta} \ln\left(\frac{\rho^{\frac{1}{3}}\Lambda}{I_0(\beta U_0)}\right) \tag{10}$$

Here ρ is the number density and $I_0(x)$ is the modified Bessel function of the first kind. Combining with eqn (8) and eqn (10), we have F for the DNA system at some fixed temperature T_0 and density. Accordingly, we can evaluate the entropy

$$S(T_0) = \frac{E(T_0) - F(T_0)}{T_0}. \tag{11}$$

We obtain S for any T by exploiting the fact that

$$C_V = T\left(\frac{\partial S}{\partial T}\right)_V = \left(\frac{\partial E}{\partial T}\right)_V, \tag{12}$$

so that

$$S(T) = \int_{T_0}^{T} \frac{1}{T}\left(\frac{\partial E(T)}{\partial T}\right)_V dT + S(T_0). \tag{13}$$

The integrand can be evaluated numerically from data for $E(T)$. Using the results for E and S, we obtain F at any T.

4 Effect of the system type: single *versus* binary NP type

In this section, we compare the thermodynamic stability of crystals formed either by the NP1–NP1 or NP1–NP2 systems. We focus on a single value for the number of linkers $\ell = 4$ and number of spacers $s = 2$. In the next section we will explore variable ℓ and s values.

4.1 FCC crystals

We start by evaluating the stability upon heating systems initially prepared with FCC crystal symmetry. For the NP1–NP1 case, an initially prepared FCC configuration is kinetically stable at low enough T. In other words, on the time scale of the simulation, dsDNA breaking and reforming is not possible, so the structure remains intact. We heat this initial crystal state to test the limits of its kinetic stability. Fig. 4 shows the potential energy per NP as a function of T. The melting is apparent from a jump in energy. To confirm the melting to an amorphous state, we compute the static structure factor

This journal is © The Royal Society of Chemistry 2011

ART ■ C0SM00989J

$$S(\vec{q}) = \frac{1}{N_{NP}}\left\langle \sum_{j=1}^{N_{NP}} \sum_{k=1}^{N_{NP}} \exp\left[i\vec{q}.(\vec{r}_j - \vec{r}_k)\right] \right\rangle, \qquad (14)$$

at each value of T, so that we can check for the presence of Bragg peaks indicating FCC structure (Fig. 4). In eqn (14), the sum is over the NP, $\vec{r}_j$ and $\vec{r}_k$ are the instantaneous coordinates of the NP centers, $\vec{q}$ is the wave vector, and $\langle \ldots \rangle$ represents the average over equilibrium configurations. We confirm that the system melts in the range $0.124 \leq T \leq 0.125$ on heating, which we refer to as the kinetic melting temperature T_M^k. We distinguish T_M^k from the thermodynamic melting temperature T_M, since, at this point, we cannot guarantee that the crystal is the most thermodynamically-stable state.

We also identify melting in two more ways which will be useful to rapidly identify melting in the other systems we examine. From the behavior of $S(q)$ (Fig. 4 (insets)), it is apparent that the amplitude of the crystal peaks change dramatically on melting. Therefore, one should be able to identify melting simply from the T dependence of any peak. In practice, we find that the third peak of $S(q)$ located at $q_2 = 1.68$ provides the most clear indication of melting (Fig. 5(a)). Since the discontinuity in the energy can be potentially difficult to distinguish from the T dependence of the energy, another convenient way to numerically locate T_M^k is *via* the specific heat

$$C_V = \left(\frac{dE}{dT}\right)_V = \frac{1}{kT^2}(\Delta E^2), \qquad (15)$$

which we can calculate both from the numerical derivative of $E(T)$ and directly from the fluctuations $\Delta E^2 = \langle E^2 \rangle - \langle E \rangle^2$ from each simulation. In principal, C_V has a discontinuity upon melting. Due to the finite intervals that we simulate, C_V instead shows a peak when the crystal melts (Fig. 5(b)).

We next directly evaluate the thermodynamic T_M of the crystal to compare with the kinetic T_M^k. To do so, we evaluate S and F for both the crystal on heating and the amorphous system on cooling, following the procedure outlined in section 3. Fig. 6 shows sample results for the FCC lattice. We confirm that the crystal

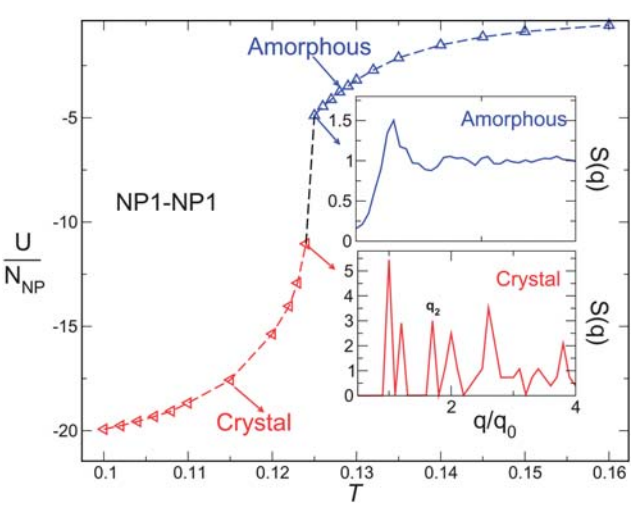

Fig. 4 Potential energy per NP as a function of T for an FCC lattice with $L = 6$, and $\ell = 4$. Melting occurs at the jump in U/N_{NP} in the range $0.124 \leq T \leq 0.125$. The insets are the structure factor $S(q)$, which confirms T_M. q_0 is the first peak of $S(q)$, and q_2 denotes the third peak of $S(q)$, discussed in Fig. 5.

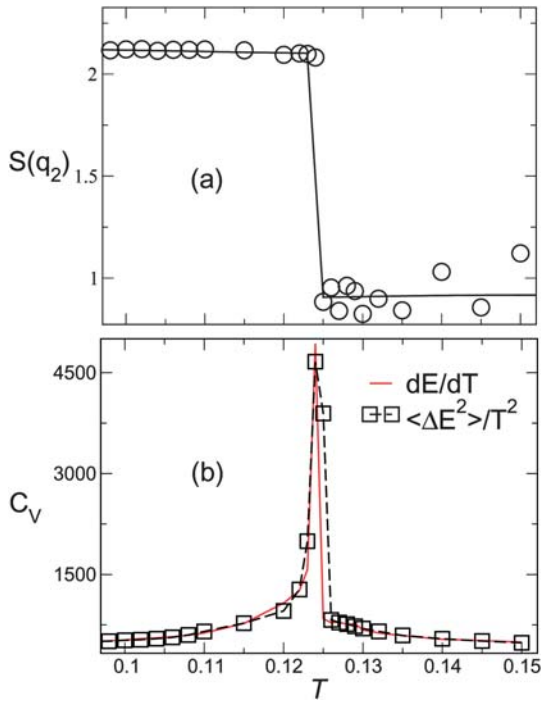

Fig. 5 Example calculation of T_M^k for an FCC lattice with $L = 6$, and $\ell = 4$ of: (a) The value of structure factor at the third peak $S(q_2)$ as a function of T; the discontinuity marks the melting transition at T_M^k. (b) T_M^k is identified by a discontinuity in the specific heat C_V, which we compute *via* the numerical derivative of $E(T)$ (solid line) and directly from the fluctuations of $E(T)$ (dashed line).

does in fact have a lower free energy than the amorphous state at low T, and hence is thermodynamically stable. The crossing point of F for the two phases indicates the location of the thermodynamic melting transition $T_M = 0.1243$. We find that T_M^k nearly coincides with T_M, so that the metastability of the crystal does not appear to play a significant role determining T_M^k. This is consistent with crystal melting due to the unzipping of strands, since the zipper transition does not exhibit hysteresis.

For the NP1–NP2 interaction, we analyze the two following cases: First we consider a 50/50 binary NP1–NP2 mixture, where two elements of the FCC unit cell are NP1 and the other two are NP2. For this case, the crystal immediately melts once the NP are not artificially fixed in location, since the checkerboard structure is incompatible with making the FCC linkages. We also consider a 25/75 binary NP1–NP2 mixture, where one element of the FCC unit cell is NP1 and the three are NP2 so that 50% of FCC linkages can in principle be formed. The latter structure, after removing the constrains, is kinetically and thermodynamically stable upon heating. We compare the stability of the 25/75 binary NP1–NP2 mixture with the NP1–NP1 and we find that the latter has (by $\approx$3%) a greater T_M and (by $\approx$50%) a greater $\Delta S(T_M)$ (Table 2). This difference appears due to the fact that the 25/75 lacks many bonds. Therefore, in the next section we will present the results of FCC lattices with only NP1–NP1 interactions.

4.2 BCC crystals

Next we turn our attention to the case of initially prepared BCC crystals. Experimentally, NP1–NP2 interactions have been

ART ■ C0SM00989J

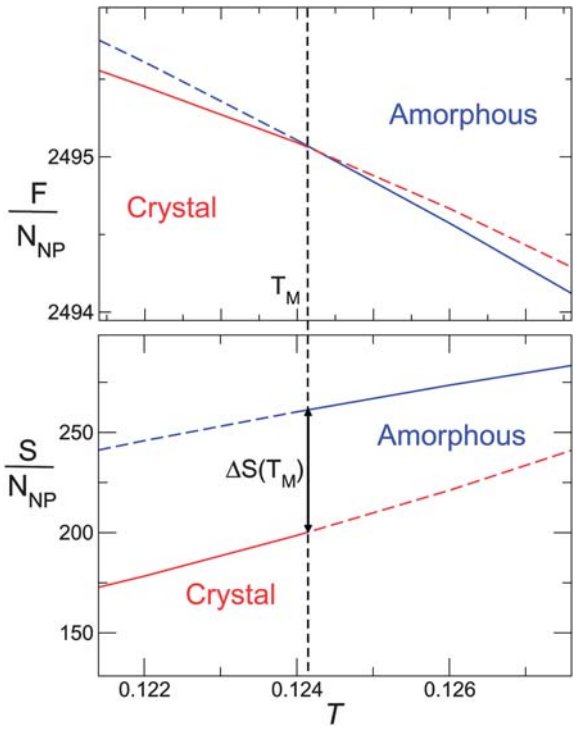

Fig. 6 Example calculation of free energy F (top panel) and entropy S (bottom panel) as a function of T for the FCC lattice. The crossing point of the amorphous and crystal free energy defines the equilibrium melting temperature $T_M = 0.1243$. The solid line represents the most stable state.

examined more frequently since it facilitates BCC formation.[25,26] However, nothing explicitly prevents BCC formation in the NP1–NP1 systems. We will take advantage of our simulations to explicitly study the properties of both the NP1–NP1 and the NP1–NP2 BCC crystal. We followed the same procedure to produce crystals as described for the FCC systems so that we may evaluate T_M^c and T_M for the BCC lattices.

From heating an initially stable BCC crystal, we find that the NP1–NP2 system has a larger T_M^c than the NP1–NP1 case, indicating that the NP1–NP2 system is more stable than the NP1–NP1 system (Fig. 7).

Curiously, we find that the energy of the crystal state of the NP1–NP1 system is less than that for NP1–NP2 at the same T (Fig. 7(a)). Since the coordination number of a BCC lattice is 8 and the NP have 12 strands, there are some ssDNA strands that do not make nearest-neighbor bonds. In the NP1–NP1 case that we study, some of these unbonded strands are able to make connections with their second neighbors (Fig. 8). The second-neighbor bonds likely facilitate the melting to an amorphous state with a significant number of DNA links. We confirm that the NP1–NP2 crystal has a larger T_M by $\approx 3\%$ and bigger

Table 2 The difference in entropy and the melting temperature for BCC and FCC lattices for the NP1–NP1 and the NP1–NP2 systems

	FCC		BCC	
	NP1–NP1	NP1–NP2	NP1–NP1	NP1–NP2
$\Delta S(T_M)/N_{NP}$	60.3	30.62	23.1	45.8
T_M	0.124	0.120	0.116	0.119

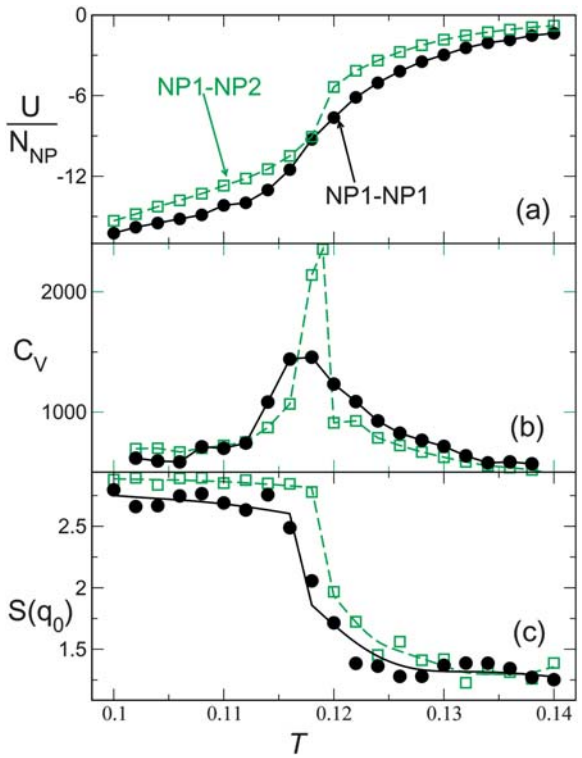

Fig. 7 Heating of an initially prepared BCC lattice with $L = 6$, and $\ell = 4$ for NP1–NP1 (filled symbols) and NP1–NP2 (open symbols) interactions: (a) The potential energy per NP as a function of T. (b) The heat capacity C_V, and (c) the structure factor at the first peak $S(q_0)$. From here, we can see that for a BCC lattice, the NP1–NP2 interaction is more stable than the NP1–NP1 interaction.

$\Delta S(T_M) \approx 50\%$, and this is thermodynamically more stable than the NP1–NP1 case (Table 2).

5 Effect of the number of bases in the spacer and linker regions

In this section, we focus our attention on the kinetic and thermodynamic stability for lattices with different numbers of spacer bases s and linker bases ℓ. For this analysis, we study only the most stable FCC (consisting of NP1–NP1) and the most stable BCC (NP1–NP2) lattices.

5.1 Numerical results

We first examine the effect of ℓ on T_M (Fig. 9). Because of the cooperativity of the zipper transition, increasing ℓ makes unzipping of the dsDNA more difficult.[44] We find that T_M increases for systems with more linkers, consistent with the crystal melting as a result of the unzipping of DNA strands, rather than a reorganization of NPs that retain linked dsDNA. Since the melting is driven by the DNA hybridization, we can understand the coincidence of the kinetic and the thermodynamic melting temperatures, since the zipper transition does not exhibit strong hysteresis. We also find the FCC crystal has a greater T_M than a BCC lattice with the same ℓ. The larger FCC coordination number z allows the NP to have more strands connected than in the BCC case, so that their are more linkages

This journal is © The Royal Society of Chemistry 2011

ART ■ C0SM00989J

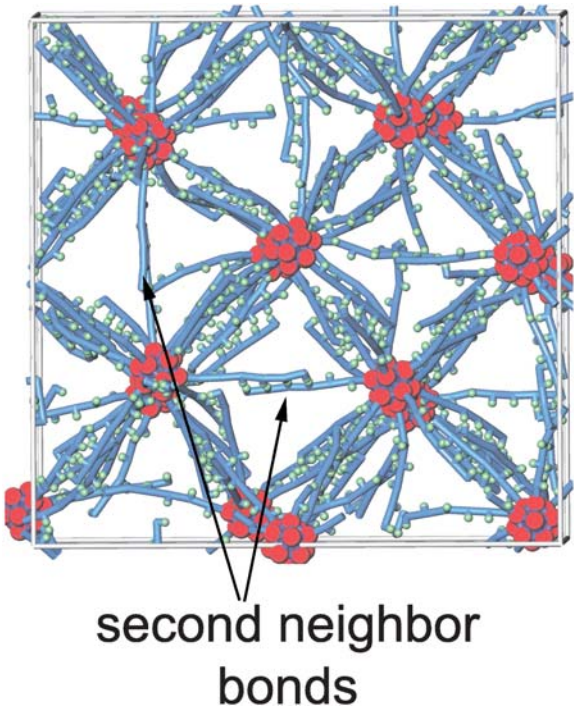

Fig. 8 A BCC lattice for the NP1–NP1 system. Some on the ssDNA that do not participate in the nearest neighbor BCC bonds are able to make connections with their second neighbors, decreasing the thermodynamic stability of the crystal.

fixing the NP positions. Finally, Fig. 9 shows that T_M decreases for systems with a longer spacer region. We next explore the origin of this effect.

In order to identify the variables that affect the stability of the crystal states, we first study how the energy of melting $\Delta U(T_M)$ changes for different ℓ and s. Fig. 10 shows that, as expected, $\Delta U(T_M)$ grows approximately linearly with ℓ. Additionally, increasing s decreases $\Delta U(T_M)$. To understand the s dependence, we recognize that any distortion of the crystal network, will place a "strain" on the dsDNA bonds. For spacer regions that are less than the ssDNA persistence length (and hence relatively rigid), increasing s places a larger torque on the dsDNA region due to distortions, such as from random thermal vibrations. Therefore, $\Delta U(T_M)$ due to melting the dsDNA bonds shrinks as s grows.

We next examine the entropy of melting $\Delta S(T_M)$. Fig. 11 shows $\Delta S(T_M)$ has a roughly linear dependence on ℓ which can be anticipated from the extensive behavior of $\Delta U(T_M)$ on ℓ. We find that $\Delta S(T_M)$ has a little dependence on the number of spacers. One might naively think that increasing s would increase the difference in entropy between the crystal and the amorphous states, and therefore make the crystal more stable upon heating. However, since the $s < l_p$, the flexibility of the strand does not change significantly by adding a small number of bases to the spacer region, and thus $\Delta S(T_M)$ is not sensitive to s.

5.2 Model for T_M

Since $T_M = \Delta U(T_M)/\Delta S(T_M)$, we combine our observations about $\Delta U(T_M)$ and $\Delta S(T_M)$ to make a simple model to describe the dependence of T_M on all control parameters. $\Delta U(T_M)$ grows linearly with ℓ, simply due the extensive nature of bonding. To

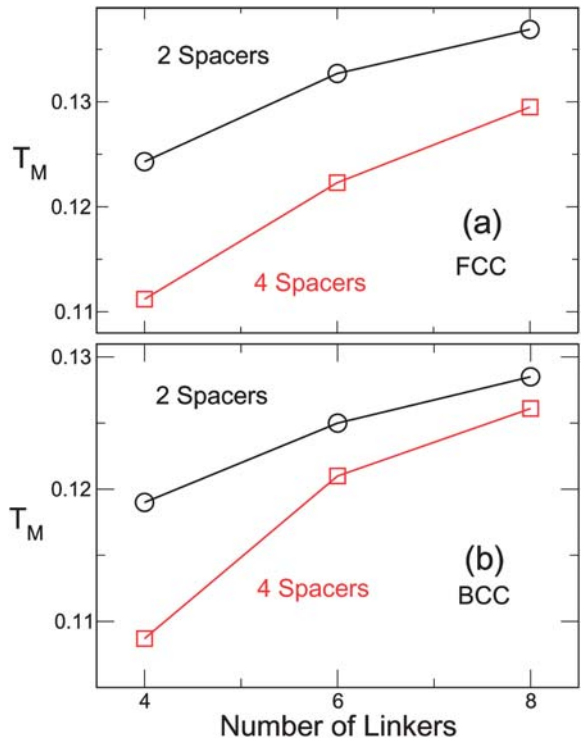

Fig. 9 The melting temperature T_M as a function of the number of linkers ℓ for (a) FCC and (b) BCC lattices with different numbers of spacers. Increasing s decreases T_M, while increasing ℓ (more linkages) increases T_M.

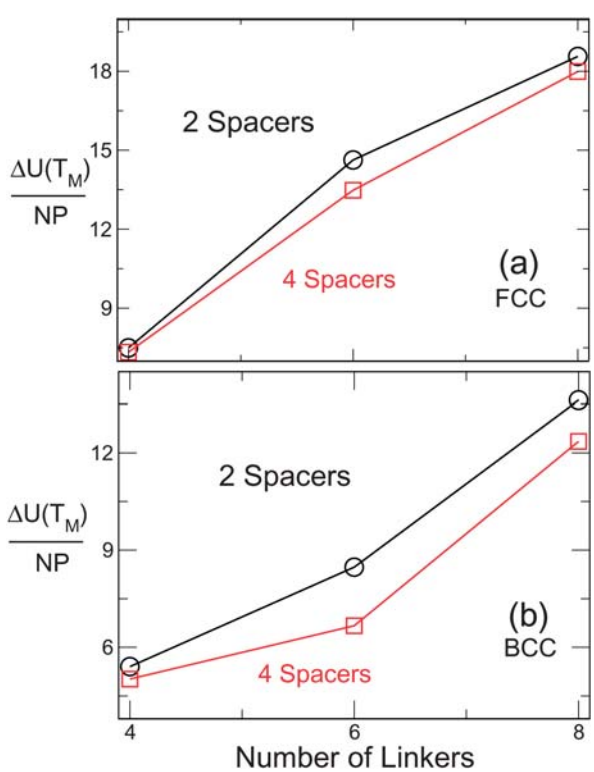

Fig. 10 The change in energy at the melting temperature T_M as a function of the number of linkers ℓ for FCC (a) and BCC (b) lattices with different numbers of spacers.

ART ■ C0SM00989J

model the decrease of $\Delta U(T_M)$, we consider that vibrations of NP from their ideal crystal positions should produce a torque on the dsDNA bonds, the strength of which will grow linearly with s. Combining these effects, we propose

$$\Delta U(T_M) = c_1 N_s \ell - c_2(s + r), \tag{16}$$

where N_s is the number of strands attached to the NP surface, r is the NP radius. We use $r + s$, the approximate total length from the NP core to the dsDNA, since changing the size of the core NP should increase the effects due to lattice distortions (although we do not test this here). Since $\Delta S(T_M)$ is linearly dependent on ℓ and is not significantly affected by s, we propose that

$$T_M = \frac{\Delta U(T_M)}{\Delta S(T_M)} = \frac{c_1 N_s \ell - c_2(s+r)}{N_s \ell}, \tag{17}$$

Using this simple model, Fig. 12 shows that T_M obtained for all values of s and ℓ examined is well described by eqn (17). In addition, we have examined the behavior of T_M for a limited set of s and ℓ values using more flexible chains (with $k_{\text{lin}} = 1$), in case the success of our model is strongly sensitive to the chain flexibility. When we decrease k_{lin}, the connection between NP are less rigid, and so we expect the NP melt more readily. Indeed we find a small decrease of T_M, by about 6–8%. Based on the logic of our model, changing k_{lin} should only affect the constant c_2 in eqn (17) associated with the weakening due to the thermal vibration. Therefore, we use the same value of c_1 found for $k_{\text{lin}} = 3$, and find agreement with eqn (17) if c_2 increases (Fig. 12). Consequently, we conclude that our model is valid even if chains are somewhat more flexible, but maintaining a spacer region less than the persistence length. The present data do not allow us to test the N_s and r dependence on eqn (17) but a subsequent paper[48] will explore these parameters.

6 Conclusion

Our molecular model for DNA-functionalized NP crystals has allowed us to test how several important control parameters can affect the crystal stability. We found that for NP functionalized with short DNA strands (6 to 12 bp), the stability of the lattices increases for systems with larger ℓ and smaller s. We found also that the NP1–NP1 interaction increases the stability of the FCC lattices and the NP1–NP2 interaction makes BCC lattices more stable. The crystal-amorphous melting is driven by the unzipping transition of the DNA strands. On the other hand, for BCC lattices with NP1–NP1 type, the crystal can melt by reorganization of the NP without a significant change in DNA linkages due to the formation of second-neighbors bonds.

Using this information, we presented a simple model which describes the melting transition as a function of the variables examined. From $S(T)$, we compute the entropy difference at T_M, which determines the heat of fusion $\Delta Q_F = T_M \Delta S(T_M)$, an indicator of the stability of the crystal relative to the amorphous state. From a design perspective, maximizing $\Delta S(T_M)$ should result in the most stable crystal state relative to the corresponding amorphous state. Although these preliminary results are encouraging for providing an understanding of the crystal stability, there are still more parameters to explore such as the number of strands attached to the NP surface, the mobility of the strands on the NP surface, and the size and geometry of the NP core, which we will study in an upcoming manuscript.[48]

In contrast with this study, most experiments[25] have examined strands which approach or exceed the strand persistence length. The behavior of these systems can potentially differ significantly. Future studies will aim bridge the understanding of the behavior of short and long DNA strands.

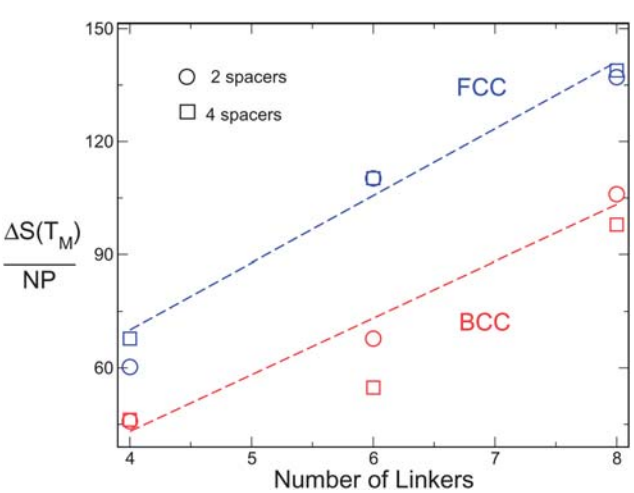

Fig. 11 Change in entropy at the melting temperature T_M for FCC and BCC lattices with different ℓ. The thermodynamic stability of the lattices depends linearly on ℓ, but it does not show significance dependence on s.

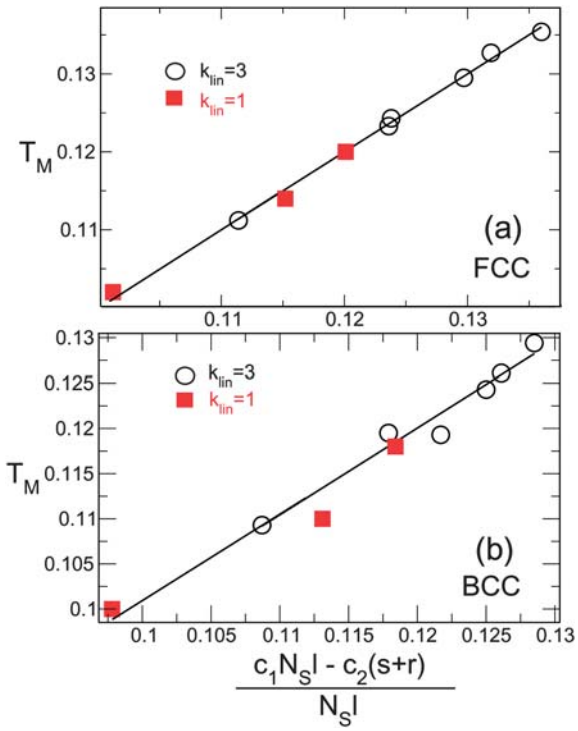

Fig. 12 Parametric plot of the numerical T_M as a function of the expected T_M from eqn (17) for (a) FCC and (b) BCC lattices. For $k_{\text{lin}} = 3$, the free constants are $c_1 = 0.148$ and $c_2 = 0.299$ for FCC; for BCC $c_1 = 0.139$ and $c_2 = 0.244$. We also consider $k_{\text{lin}} = 1$, which should only change the constant c_2 in eqn (17), and find $c_2 = 0.336$ for the FCC and $c_2 = 0.366$ for the BCC data.

This journal is © The Royal Society of Chemistry 2011

ART ■ C0SM00989J

References

1 N. Seeman, *Nature*, 2003, **421**, 427–431.
2 C. Niemeyer, *Curr. Opin. Chem. Biol.*, 2000, **6**, 609–618.
3 A. Condon, *Nat. Rev. Genet.*, 2006, **7**, 565–575.
4 C. Mirkin, R. Letsinger, R. Mucic and J. Storhoff, *Nature*, 1996, **382**, 607–609.
5 A. Alivisatos, K. Johnsson, X. Peng, T. Wilson, C. Loweth, M. Bruchez and P. G. Shultz, *Nature*, 1996, **382**, 609–610.
6 N. Geerts and E. Eiser, *Soft Matter*, 2010.
7 V. T. Milam, A. L. Hiddessen, J. C. Crocker, D. J. Graves and D. A. Hammer, *Langmuir*, 2003, **19**, 10317–10323.
8 M. Valignat, O. Theodoly, J. Crocker, W. Russel and P. Chaikin, *Proc. Natl. Acad. Sci. U. S. A.*, 2005, **102**, 4225–4229.
9 P. Biancaniello, A. Kim and J. Crocker, *Phys. Rev. Lett.*, 2005, **94**, 0583021–0583024.
10 A. J. Kim, P. L. Biancaniello and J. C. Crocker, *Langmuir*, 2006, **22**, 1991–2001.
11 P. Biancaniello, J. Crocker, D. Hammer and V. Milam, *Langmuir*, 2007, **23**, 2688–2693.
12 T. Schmatko, N. Geerts, E. Eiser and W. Poon, *Soft Matter*, 2007, **3**, 703–706.
13 N. Geerts, T. Schmatko and E. Eiser, *Langmuir*, 2008, **24**, 5118–5123.
14 A. J. Kim, R. Scarlett, P. L. Biancaniello, T. Sinno and J. C. Crocker, *Nat. Mater.*, 2009, **8**, 52–55.
15 N. Geerts and E. Eiser, *Soft Matter*, 2010, **6**, 664–669.
16 Y. Maeda, H. Tabata and T. Kawai, *Appl. Phys. Lett.*, 2001, **79**, 1181–1183.
17 S.-J. Park, A. A. Lazarides, C. A. Mirkin and R. L. Letsinger, *Angew. Chem., Int. Ed.*, 2001, **40**, 2909–2912.
18 C. Soto, M. Srinivasan and B. Ratna, *J. Am. Chem. Soc.*, 2003, **124**, 8508.
19 R. Jin, G. Wu, Z. Li, C. Mirkin and G. Schatz, *J. Am. Chem. Soc.*, 2003, **125**, 6.
20 S. Park, A. Lazarides, J. Storhoff, L. Pesce and C. Mirkin, *J. Phys. Chem.*, 2004, **108**, 12375–12380.
21 S. Park, J. Lee, D. Georganopoulou, C. Mirkin and G. Schatz, *J. Phys. Chem.*, 2006, **B110**, 12673–12681.
22 M. M. Maye, D. Nykypanchuk, D. van der Lelie and O. Gang, *J. Am. Chem. Soc.*, 2006, **128**, 14020–14021.
23 M. M. Maye, D. Nykypanchuk, D. van der Lelie and O. Gang, *Small*, 2007, **3**, 1678–1682.
24 D. Nykypanchuk, M. M. Maye, D. van der Lelie and O. Gang, *Langmuir*, 2007, **23**, 6305.
25 D. Nykypanchuk, M. Maye, D. V. der Lelie and O. Gang, *Nature*, 2008, **451**, 549–552.
26 S. Y. Park, A. Lytton-Jean, B. Lee, S. Weigand, G. Schatz and C. Mirkin, *Nature*, 2008, **451**, 553–556.
27 R. Macfarlane, B. Lee, H. Hill, A. J. Senesi, S. Seifert and C. Mirkin, *Proc. Natl. Acad. Sci. U. S. A.*, 2009, **106**, 10493–10498.
28 H. Xiong, D. van der Lelie and O. Gang, *Phys. Rev. Lett.*, 2009, **102**, 015504.
29 J. Crocker, *Nature*, 2008, **451**, 528–529.
30 O. S. Lee and G. C. Schatz, *J. Chem. Phys.*, 2009, **113**, 2316–2321.
31 F. W. Starr and F. Sciortino, *J. Phys.: Condens. Matter*, 2006, **18**, L347–353.
32 C. W. Hsu, J. Largo, F. Sciortino and F. W. Starr, *Proc. Natl. Acad. Sci. U. S. A.*, 2008, **105**, 13711–13715.
33 J. Largo, F. W. Starr and F. Sciortino, *Langmuir*, 2006, **23**, 5896–5905.
34 W. Dai, C. W. Hsu, F. Sciortino and F. W. Starr, *Langmuir*, 2010, **26**, 3601–3608.
35 T. Ouldridge, I. Johnston, A. Louis and J. Doye, *J. Chem. Phys.*, 2009, **130**, 11.
36 C. Hsu, F. Sciortino and F. W. Starr, *Phys. Rev. Lett.*, 2010, in press.
37 M. Doi and S. F. Edwards, *The Theory of Polymer Dynamics*, Clarendon Press, 1999.
38 M. Murphy, I. Rasnik, W. Cheng, T. M. Lohman and T. Ha, *Biophys. J.*, 2004, **86**, 2530–2537.
39 J. B. Mills, E. Vacano and P. J. Hagerman, *J. Mol. Biol.*, 1999, **285**, 245–257.
40 B. Tinland, A. Pluen, J. Sturm and G. Weill, *Macromolecules*, 1997, **19**, 5763–5765.
41 T. Ouldridge, A. Louis and J. Doye, *Phys. Rev. Lett.*, 2010, **104**, 178101.
42 T. Knotts, N. Rathore, D. Schwartz and J. de Pablo, *J. Chem. Phys.*, 2007, **126**, 084901.
43 P. Dans, A. Zeida, M. Machado and S. Pantano, *J. Chem. Theory Comput.*, 2010, **6**, 1711–1725.
44 J. SantaLucia, *Proc. Natl. Acad. Sci. U. S. A.*, 1998, **95**, 1460–1465.
45 D. Frenkel and B. Smit, *Understanding Molecular Simulation*, Academic Press, 2nd edn, 2001.
46 M. Tuckerman, B. J. Berne and G. J. Martyna, *J. Chem. Phys.*, 1992, **97**, 1990–2001.
47 S. Sastry and F. Sciortino, personal communication, 2010.
48 O. Padovan-Merhar, F. Vargas-Lara and F. W. Starr, preprint, 2010.

ART ■ C0SM00989J